BEHAVIOUR OF Rh SUPPORTED ON HYDROXYAPATITE CATALYSTS IN PARTIAL OXIDATION AND STEAM REFORMING OF METHANE: ON THE ROLE OF THE SPECIATION OF THE Rh PARTICLES

Z. Boukha, A. Choya, M. Gil-Calvo, B. de Rivas, J.R. González-Velasco,
J.I. Gutiérrez-Ortiz, R. López-Fonseca

Applied Catalysis A, General 526 (2018) 191-203

DOI: 10.1016/j.apcata.2018.03.002

Behaviour of Rh supported on hydroxyapatite catalysts in partial oxidation and steam reforming of methane: On the role of the speciation of the Rh particles

Zouhair Boukha, Miryam Gil-Calvo, Beatriz de Rivas, Juan R. González-Velasco, José I. Gutiérrez-Ortiz, Rubén López-Fonseca

Chemical Technologies for Environmental Sustainability Group, Department of Chemical Engineering, Faculty of Science and Technology, University of the Basque Country UPV/EHU, P.O. Box 644, E-48080 Bilbao, Spain

*Corresponding author: Zouhair Boukha

Phone: +34 946015502

Fax: +34 946013500

E-mail address: zouhair.boukha@ehu.eus

Abstract

Rh/hydroxyapatite samples were prepared by impregnation and investigated for the partial oxidation (POM) and steam reforming (SRM) of methane. The catalysts were analysed by BET, XRD, DRS, XPS, H_2-TPR, TEM, H_2 chemisorption, CO_2-TPD and NH_3-TPD techniques. The characterisation results showed that, after calcination, Rh existed in three different forms in the samples: (i) large crystallites of Rh_2O_3 deposited on the surface of the catalysts, (ii) RhO_x in small particles exhibiting strong interaction with the support and (iii) a phase of Rh^{2+} species which incorporated the hydroxyapatite framework.

Operating in the POM and SRM processes the reduced Rh(x)/HAP catalysts resulted highly active and exhibited excellent stability at 973 K (for 30 h). This behaviour was explained by their high coke-resistance. The activity of the catalyst with the optimum loading (1%), in SRM, was compared with that of a commercial Rh/Al_2O_3 catalyst. The conversion and H_2 and CO yields values achieved on the former were all close to those exhibited by the latter. This comparable behaviour was explained by suitable properties provided by the HAP support such as reducibility, lower surface acidity and larger pore sizes (ensuring a better diffusion of the reactants and the products during the SRM reaction). These properties seemed to compensate the low dispersion of the Rh active phase induced by its low specific surface area.

Keywords: Hydroxyapatite, Rh species, methane, partial oxidation, steam reforming.

1. Introduction

Currently, the technologies applied for methane reforming for synthesis gas production consist of steam reforming (SRM), partial oxidation (POM) and oxidative steam reforming (OSRM) [1]. The choice of the appropriate technology is based on the posterior use of the synthesis gas (H_2 and CO). For instance, hydrogen for fuel cell applications is mainly produced by the endothermic SRM (1), providing high H_2/CO ratio (≥ 3), before its subsequent purification. However, the exothermic POM (2) is the suitable technology for Fischer-Tropsch synthesis which requires a syngas mixture with H_2/CO ratio close to 2. Furthermore, for many applications OSRM is a strategy of choice where SRM and POM processes could be efficiently coupled [1]. By adjusting the O/C ratio of the inlet gas mixture the latter strategy can allow the control of the process heat and the distribution of the products.

$$CH_4 + H_2O \rightarrow 3H_2 + CO \qquad \Delta H^o_{298K} = +206 \text{ kJ mol}^{-1} \qquad (1)$$

$$CH_4 + \tfrac{1}{2} O_2 \rightarrow 2H_2 + CO \qquad \Delta H^o_{298K} = -36 \text{ kJ mol}^{-1} \qquad (2)$$

For methane reforming processes, Ni and a variety of noble metals (Ru, Rh, Pd, Ir, Pt) are used as the active phases. For economic considerations, Ni is the most widely used; however, it presents high susceptibility to sintering which causes coke deposition and, then, a deactivation of its active sites [1-4]. Though many formulations were investigated in order to enhance their dispersion, the stability of Ni catalysts is still lower than that exhibited by the noble metals. This is because of their low specific activity which requires the preparation of catalysts with high Ni loadings (> 15%) [1-4]. Among the noble metals, Rh has been found to be an excellent catalyst for the methane reforming reactions. Data from the literature show that over the Rh catalysts the values

of the activation energy for POM (38-55 kJ mol^{-1}) are significantly lower than for SRM (109 kJ mol^{-1}) [5].

Usually, the Rh active phases are supported on chemically active or inert metal oxides presenting high specific surface area. Besides their high initial activity, the Rh catalysts prove a very good stability due to their high resistance against carbon formation, even in the demanding dry reforming process [6]. In order to improve, even more, the performance of the Rh catalysts, current research is mainly focused on the examination of the influence of the nature of the support on their activity and selectivity. In this sense, Rh was deposited on various materials, such as Al_2O_3, TiO_2, CeO_2, MgO, La_2O_3, SiO_2, ZrO_2 and ZSM-5 with the aim of finding suitable interactions metal-support [5,7,8]. According to many reports, irrespective of the employed oxidant (O_2 or H_2O), the methane reforming activity is sensitive to the type of these interactions which strongly affect the Rh dispersion, its oxidation state and the acid-base properties of the surface [5, 9, 10]. However, the nature of the active Rh species in POM is a subject of controversy. For instance, in their study on the Rh/Al_2O_3 catalysts Buyevskaya et al. [11] found that a high degree of surface reduction was necessary for high hydrogen yield. By contrast, other reports showed that during POM at 973 K the Rh active species consist of the metallic crystallites and partially reduced oxide clusters dispersed in the rhodium metal matrix [12].

In their study on the activity of Rh/MgO-Al_2O_3 catalysts in SRM reaction Wang et al. [13] reported that CH_4 turnover rate decreased with increasing Rh crystallite size evidencing the structure sensitivity towards methane steam reforming over the range of Rh crystalline size examined (5-15 nm). Ligthart et al. [10] studied the influence of Rh particle sizes (using ZrO_2, CeO_2, $CeZrO_2$ and SiO_2 as supports) on the catalytic performance in SRM. They pointed out that the nature of the support influenced the

dispersion and the reduction degree of the metal phase. They also observed that, irrespective of the used support, catalysts with Rh nanoparticles smaller than 2.5 nm deactivated more strongly than catalysts with larger nanoparticles. The observed deactivation was explained by the oxidation of very small particles of Rh under the SRM conditions.

In the present work, we investigate the textural, structural and chemical properties of a series of Rh/hydroxyapatite catalysts for their application in two methane reforming processes (POM and SRM). We chose hydroxyapatite (HAP: $Ca_{10}(PO_4)_6(OH)_2$) for study because of its interesting characteristics and catalytic properties. It is known that HAP can form synergistic interactions with a variety of transition metals because of its high ion-exchange capacity [14-19]. Moreover, the apatite structure tolerates large deviation from stoichiometry. For instance, Ca-deficient hydroxyapatite exhibits peculiar structural rearrangement for charge compensation with formation of cation (Ca^{2+}) and anion (OH^-) vacancies. Despite of the fact that a number of studies dealing with HAP support are presently available, to the best of our knowledge, the catalytic properties of Rh/HAP samples in the POM and SRM reactions have not been yet investigated.

2. Experimental

Non-stoichiometric hydroxyapatite support (HAP) was synthesised using a protocol reported elsewhere [14-19]. The Rh/HAP catalysts were prepared by impregnation using solutions containing three different amounts of $RhCl_3{\cdot}3H_2O$ precursor. The impregnated samples were dried in air at 120 °C for 12 h and subsequently calcined for 4 h, at 1000 K. The obtained samples will be hereafter referred as Rh(x)/HAP (x = 0.5, 1 and 2wt.%).

The characterisation of the prepared samples involved a wide number of techniques including BET, TEM, XRD, H_2-TPR, DRS, XPS and volumetric adsorption of NH_3 and CO_2 (at 313 K) as well-known probe molecules for acid and basic sites, respectively. The experimental details of each analytical technique are described elsewhere [14-16].

The morphology, size and dispersion of the rhodium particles on the reduced Rh(x)/HAP were analysed by transmission electron microscopy. The corresponding experiments were performed on a Philips CM200 transmission electron microscope equipped with LaB6 filament operating at 200 kV and combined with X-ray energy dispersive spectroscopy (X-EDS) techniques. The average diameter calculations of the rhodium particles were made from the measurement of at least 150 particles using ImageJ software. The values of Rh dispersion and metallic surface area were calculated according to a procedure described by Borodzinski and Bonarowska. [20].

The dispersion of the Rh particles was also determined by H_2 chemisorption techniques. The experiments were carried out on Micromeritics AutoChem 2920 instrument equipped with a thermal conductivity detector (TCD). The catalysts (100 mg) were submitted to a reduction at 1000 K (1 h) in a flow 5%H_2/Ar (50 cm^3 min^{-1}) before cooling to 313 K under Ar. H_2 pulses (5%H_2/Ar, loop volume: 0.5 cm^3) were then injected in Ar carrier (50 cm^3 min^{-1}) over the sample, at 313 K. The Rh dispersion, D, defined as the active metal fraction exposed was determined on the assumption of a unity adsorption stoichiometry (H/Rh = 1). The average size of the Rh particles was calculated, assuming that Rh particles have a spherical shape, from the following equations [20]:

i) For low Rh dispersion (< 20%): $d(nm) = 1.34/D$ (3)

ii) For high Rh dispersion (≥ 20%): $d(nm) = 0.89/D^{1.23}$ (4)

The POM and SRM catalytic tests over the Rh(x)/HAP catalysts were performed, with the same gas hourly space velocity (GHSV), 19,200 cm^3 CH_4 g^{-1} h^{-1}, in a tubular flow reactor operating at atmospheric pressure, using 250 mg of the catalyst and a total feed gas mixture of 800 cm^3 min^{-1}. For comparison, the activity of a commercial Rh/Al_2O_3 catalyst with 1% Rh (Alfa Aesar) was also studied. For the POM reaction experiments the reactive gas mixture was composed of 10% CH_4 and 5% O_2 (O/C = 1) balanced with N_2. The SRM catalytic tests (H_2O/C = 3) were performed with a feed gas mixture composed of 10%CH_4 and 30%H_2O balanced with N_2. Prior to running the experiments, the catalysts were submitted to a high-temperature reduction step at 1000 K (1 h) in a flow 5%H_2/N_2. The temperature of the reaction was increased from 773 K to 1000 K with a heating rate of 3 K min^{-1}. In order to investigate the stability of the catalysts, additional experiments were carried out at a constant temperature (973 K) for about 30 h. The reaction products were continuously analysed by a gas chromatograph equipped with a TCD detector. Methane conversion and H_2, CO and CO_2 yields ($X(CH_4)$, $Y(H_2)$, Y(CO) and $Y(CO_2)$, respectively) were calculated by using the corresponding inlet and outlet molar flow values (Eqs. (5), (6), (7) and (8), respectively):

$$X\left(CH_4\right),\% = \frac{F\left(CO,_{out}\right)+F\left(CO_2,_{out}\right)}{F\left(CH_{4,in}\right)}\cdot 100 \tag{5}$$

$$Y(H_2) = \frac{F(H_{2,out})}{2\cdot F(CH_{4,in})} \tag{6}$$

$$Y(CO) = \frac{F(CO_{,out})}{F(CH_{4,in})} \tag{7}$$

$$Y(CO_2) = \frac{F(CO_{2,out})}{F(CH_{4,in})} \tag{8}$$

The thermodynamic data were calculated via the HSC Chemistry software package by the GIBBS programme using the so-called Gibbs Energy Minimization Method. The substances to be taken into account in the calculations, the amount of reactants, the potentially stable phases as well as the temperature of raw species were specified as input. In addition to solid carbon, the following substances in the gas phase were considered: CH_4, O_2, N_2, CO, CO_2, H_2 and H_2O.

3. Results and discussion

3.1. N_2-physorption (BET measurements)

The N_2 physisorption isotherms recorded at 77 K for the support and the three Rh samples are included as supplementary material (Fig. S1). The observed isotherms and the hysteresis loops typology of all catalysts were similar. Data obtained from the analysis of the isotherms corresponding to the calcined and reduced samples are summarised in Table 1 and Fig. 1. The pore size distribution of the HAP bare support consisted of a broad peak centred at 53 nm. Interestingly, after reduction, the latter became narrower and shifted towards lower value (38 nm). This behaviour could be associated with structural changes induced by the reduction process. Regarding the effect of the Rh content on the specific surface area, a slight decrease in the S_{BET} was observed on the reduced Rh(0.5)/HAP (26 m^2 g^{-1}) and Rh(2)/HAP (25 m^2 g^{-1}) catalysts when compared with that measured on the HAP bare support (33 m^2 g^{-1}). By contrast, the deposition of 1% Rh did not induce a significant change in the S_{BET}, which was around 30 m^2 g^{-1}. The difference between the three Rh catalysts might be related with a distinct evolution of the surface phases and/or the dispersion of the Rh species. In parallel, as reported in Fig. 1, the progressive addition of Rh induced a significant increase in the broadness of the peak around 50 nm. The curves corresponding to the

Rh(1)/HAP and Rh(2)/HAP catalysts also showed a shoulder between 30-40 nm indicating an heterogeneity of their surface. Nevertheless, when reduced at 1000 K, all Rh samples did not show significant changes in their pore size distribution.

3.2. X-ray diffraction (XRD)

The XRD diagrams of the Rh(x)/HAP samples compared with that of HAP bare support are shown in Fig. 2. The indexation of the diffraction peaks of the synthesised HAP sample confirmed the formation of a unique phase, identical to hydroxyapatite structure (JCPDS 01-082-2956). The estimation of the average size of the HAP particles, by means of Scherrer equation, showed that it was around 49 nm. Moreover, its degree of crystallinity was estimated to be around 0.98. The latter value was significantly higher than that reported in our previous study on HAP samples calcined at 773 K which was around 0.80 [16]. This improvement in the cristallinity of the HAP with the increase of the calcination temperature was in good agreement with the results found by Kim et al. [21]. After reduction of HAP support at 1000 K the structure remained unchanged; however a significant decrease in the crystallite size, from 49 to 32 nm, could be noted (Table 1). This evolution could explain the observed shift in the pore size distribution towards lower values (Fig. 1). This effect was also accompanied by a slight decrease in the HAP lattice parameters. This corresponded to a lattice reduction of the apatite structure of about 0.1%. Since the reduction of Ca^{2+} was discarded, the observed change was associated with a possible increase in the density of the oxygen vacancy [22-23]. According to Bystrov et al. [23] there are various possible oxygen vacancies in the apatite lattice: O from PO_4, O from OH, the loss of an entire OH group, or the simultaneous loss of O from PO_4 and an entire OH group.

As expected, due to its low concentrations (≤ 2%), the diffractograms of Rh-doped HAP catalysts, in their oxidised and reduced forms, showed no lines attributed to Rh phases (Fig. 2). However, a clear evolution in the positions of the HAP diffraction peaks, with Rh addition could be noticed (Fig. 2); thereby suggesting a modification in the cell parameters of the HAP crystal. Table 1 lists the corresponding values calculated for all Rh(x)/HAP samples. The reported data revealed a significant increase in the "a" parameter and the volume of the lattice with increasing the Rh content which could be attributed to a possible incorporation of Rh species into the HAP framework. Since the ionic radius of Rh (0.20 nm) is smaller than that of Ca (0.23 nm), the observed expansion was explained by an incorporation of Rh into the cationic vacant sites rather than an ion-exchange process with Ca^{2+} sites. A similar observation could be found in our previous study dealing with Pd/HAP samples [16]. After reduction the Rh(x)/HAP patterns showed the presence of an additional peak at 30.7º with a low intensity. Interestingly, this feature was more pronounced in the case of the Rh(0.5)/HAP and the Rh(2)/HAP samples. A comparison of the observed peak with reference data evidenced a transformation of a small fraction of the hydroxyapatite structure into tricalcium phosphate (TCP: $Ca_3(PO_4)_2$) phase (JCPDS 00-009-0348). This effect could be explained by a possible acceleration of HAP→TCP transition due to the reduction of the Rh species incorporating the HAP framework. A more careful analysis of the patterns of the Rh(2)/HAP sample revealed that the intensity ratio (I_{TCP}/I_{HAP}) of the most intense peaks corresponding to $TCP_{(170)}$ and $HAP_{(211)}$, respectively, differed from that of Rh(0.5)/HAP and Rh(1)/HAP catalysts. Indeed, the value of this ratio was about 5.2% for the Rh(1)/HAP, 6.2% for the Rh(0.5)/HAP; whereas it increased up to 9% for the Rh(2)/HAP catalyst. The high contribution of the TCP phase in the latter could be associated with the incorporation of large amounts of Rh in the HAP framework.

Moreover, we thought that this structure transformation might be responsible for the loss in the S_{BET} noticed, especially, for the Rh(0.5)/HAP and Rh(2)/HAP catalysts.

3.3. Temperature programmed reduction (H_2-TPR)

H_2-TPR experiments were carried out in order to investigate the reducibility of the HAP support and the different Rh species (Fig. 3). The diagram of the bare support was characterised by the presence of an intense peak centred at 705 K with a H_2 uptake around 209.1 μmol g^{-1}. According to many reports, the latter was probably due to the consumption of surface oxygen anions species [24-27]. Moreover, these species could be restored by a simple reoxidation of the sample [27]. In order to evaluate this possibility the HAP sample was subjected to a second H_2-TPR experiment after its reoxidation at 1000 K (Fig. S2). The results evidenced a striking similarity between the two successive H_2-TPR profiles in terms of the peak position and the H_2 uptake, thus confirming the reversibility of the redox process.

Besides the HAP reduction peaks, the H_2-TPR profiles corresponding to the Rh catalysts were characterised by the presence of additional uptakes due to the reduction of at least three different species of Rh. At low temperatures, < 600 K, the spectra showed two peaks, named α and β, in the temperature ranges of 445-460 K and 490-550 K, respectively. Generally, the presence of the former is associated with the reduction of supported Rh_2O_3 species whereas the latter could be attributed to the reduction of Rh species exhibiting a relatively mild interaction with the support [28-30]. On the other hand, the peak at significantly higher temperatures (γ), > 873 K, was due to the reduction of the Rh species presenting much stronger interactions with the support. The occurrence of such feature was found in previous studies on different systems [28-30]. For instance, Ruckenstein et al. [28] observed in the reduction spectra of Rh/La_2O_3,

Rh/MgO, Rh/Y_2O_3 and Rh/Ta_2O_5 a high temperature peak associated with the reduction of $LaRhO_3$, $MgRh_2O_4$, $YRhO_3$ and $RhTaO_4$ species, respectively. Moreover, Rice et al. [31] evidenced the stability of Rh^{2+} ions species in the framework of ZSM-5 occupying sites located in the walls of the channels. The presence of stable Rh^{2+} species was also suggested in the case of Rh/Al_2O_3 systems when rhodium diffuses into the support forming a rhodium spinel [32]. Therefore, in good agreement with these previous studies, the high temperature peak observed in our H_2-TPR profiles could be assigned to Rh^{2+} species which incorporated the hydroxyapatite network. This conclusion was supported by analysing the values of H_2/Rh molar ratios determined by the integration of all Rh reduction peaks (Table 2). Indeed, the corresponding values (1.2-1.3) showed that they were lower than those expected for a complete reduction of Rh^{3+} in Rh_2O_3 species (1.5) thereby the presence of a fraction of Rh with a lower oxidation state (probably Rh^{2+}). It should be noted that this possible incorporation of Rh was also assessed by XRD techniques.

Table 2 also reports the quantification of H_2 uptake corresponding to α, β and γ species. The results revealed that the distribution of Rh species among the different sites did not depend on the Rh content. For instance, the incorporated amounts of Rh exhibited the lowest contribution (17%) on the Rh(1)/HAP sample, whereas they presented higher values on the Rh(0.5)/HAP (26%) and Rh(2)/HAP (22%). This suggested that these two samples were more prone to incorporate the Rh into the HAP structure. It is also worth nothing that this difference could explain the resistance of the Rh(1)/HAP sample against the loss in surface area.

3.4. X-ray photoelectron spectroscopy (XPS)

The chemical composition and the distribution of the Rh species laying on the surface of the calcined Rh(x)/HAP catalysts were investigated by means of XPS techniques. Fig. 4 and Table 3 summarise the corresponding results. The value of the surface Ca/P atomic ratio of the bare support (1.5) was in good agreement with the bulk analysis (Table 3). Among all Rh catalysts, the Rh(0.5)/HAP sample presented an exception since it exhibited a slightly higher Ca/P ratio (1.6). This suggested that the Ca species were more exposed to the surface than the other two samples. Previous studies have evidenced a direct relationship between the variation in the Ca/P ratio and the drastic changes in the chemical properties of the hydroxyapatite [33]. The effect of the observed Ca/P increase on the acid-base properties of the prepared materials will be commented below.

The XPS spectra of all Rh(x)/HAP catalysts, in the Rh $3d_{5/2}$ and Rh $3d_{3/2}$ regions, displayed two main peaks centred at 307.8 ± 0.1 eV and 312.4 ± 0.2 eV, respectively (Fig. 4 and Table 3). Besides the occurrence of Rh^{3+} species, these values revealed the presence of Rh^{2+} species; since the corresponding binding energy were peaked between that of Rh^{0} (307 eV) and Rh^{3+} (308.1-308.6) states [32,34]. Nevertheless, the position of these features seemed to depend, systematically, on the Rh content. For instance, in the spectrum of the sample with the lowest Rh loading (0.5%) the observed $3d_{5/2}$ peak was centred at 307.9 eV; whereas it shifted towards lower binding energies in the case of the Rh-rich samples (307.8 eV for Rh(1)/HAP and 307.7 eV for Rh(2)/HAP). As reported in previous studies [15], this negative shift of the core level spectra was consistent with a decrease in the metal-support interaction with an increased Rh loading. Moreover, the calculated difference between the energy positions corresponding to $3d_{3/2}$ and $3d_{5/2}$ peaks also evidenced a systematic variation in the spin-orbit splitting (4.7 eV for

Rh(0.5)/HAP, 4.6 eV for Rh(1)/HAP and 4.5 eV for Rh(2)/HAP). Table 3 also compares the concentrations of Rh determined in the bulk (ICP) and the near surface (XPS) of the catalysts. Exclusively, the Rh(2)/HAP sample exhibited a lower surface Rh amount (1.4%) compared with that determined by ICP (2%), thus suggesting a low dispersion of the Rh particles.

3.5. Diffuse reflectance spectroscopy (DRS)

Diffuse reflectance spectroscopy was used to study the symmetry and the coordination of rhodium species dispersed on the HAP support. Fig. 5 displays the optical absorption spectra, for the oxidised Rh(x)/HAP catalysts, recorded in the range 200-1200 nm. For the sake of comparison, the spectrum of the Rh(2)/HAP sample reduced at 773 K was also included. The attribution of the absorption bands was carried out by comparison with spectra of earlier studies dealing with rhodium complexes [35-43].

It is known that the trivalency is definitely the most stable oxidation number among Rh ions in oxides [35]. The typical spectrum of Rh^{3+} ($4d^6$) is composed of two bands in the visible domain describing two allowed d-d transitions ($^1A_{1g} \rightarrow {}^1T_{1g}$ (at 535 nm) and $^1A_{1g} \rightarrow {}^1T_{2g}$ (at 420 nm)) [35,36,43]. The Rh^{2+} ($3d^7$) ions also exhibit a simple spectrum that involves two d-d transitions ($^2E_g \rightarrow {}^2T_{1g}$ and $^2E_g \rightarrow {}^2T_{2g}$) appearing in the visible domain. Groller-Walrand et al. [43] evidenced, experimentally, the absorption of these features, having approximately the same energy, between 500-600 nm. Rh^{4+} ($4d^5$) and Rh^{5+} ($4d^4$), however, when doped into oxide matrices give, besides the visible region bands between 400-800 nm, an absorption band in the NIR wavelength region [37,41,42]. In their study on the evolution of the oxidation states of Rh, Kaczmarek et al. [37] attributed the absorption around 650 nm to Rh^{4+} species and around 800 nm to Rh^{5+} species. Furthermore, according to many reports, the existence of two Rh

oxidation states induces an interaction between their respective sites and leads to additional absorption bands due to metal to metal charge transfer in the visible and/or NIR domain [35,38,42].

The spectrum of HAP bare support exhibited a weak band centred at 310 nm which was assigned to Ca-O charge transfer [15, 16]. Interestingly, the visible region was characterised by the presence of two bands at 520 nm and 740 nm. The occurrence of the latter was in good agreement with the optical bands attributed to the presence of OH vacancy in the hydroxyapatite structure [23]. This result was expected since the prepared support presented a deficiency in Ca^{2+} which was probably compensated by the addition of H^+ and/or removal of OH^- ions [15].

The spectra of Rh(x)/HAP catalysts were characterised by the presence of a weak band at 220 nm attributed to Rh-O charge transfer [36,40] and a broad asymmetric band in the visible region. The latter seemed to be broader on the Rh(0.5)/HAP and Rh(2)/HAP spectra compared with that of the Rh(1)/HAP. Interestingly, in good agreement with the H_2-TPR and XPS results, the absence of high wavelength bands (above 650 nm) demonstrated that Rh^{3+} and/or Rh^{2+} were the dominant valence states. It should be noted that, as the concentration of Rh increased, the samples colour changed from light pink-brown for Rh(0.5)/HAP to dark gray-brown for Rh(1)/HAP and dark gray (which is typical of the Rh_2O_3 species) in the case of Rh(2)/HAP. The observed changes indicated an apparent abundance of bulk Rh_2O_3 with Rh loading. In order to confirm the presence of the Rh^{2+} species incorporated in the HAP structure the Rh(2)/HAP sample was reduced at 773 K and then analysed by DRS. We assumed that this temperature was sufficiently high for reduction of all Rh^{3+} species while the incorporated Rh species could keep their cationic form (Rh^{2+}). Indeed, as shown in Fig. 5, the corresponding spectrum only showed an absorption band in the visible region, centred at 575 nm,

evidencing the presence of Rh^{2+} species [43]. This was actually a relevant observation, not reported as yet, which confirmed that DRS is, indeed, a powerful tool providing valuable information about the nature of the ionic species of Rh.

3.6. Morphology and dispersion of the Rh particles

Hydroxyapatite-supported rhodium samples, reduced at 1000 K, were investigated by TEM techniques. Fig. 6 displays the corresponding TEM images and the particle size distribution traces. Examination of the Rh(0.5)/HAP sample revealed the presence of spherical Rh particles dispersed on the support surface. Furthermore, the corresponding size distribution diagram consisted of a broad distribution with an average size of 12.8 nm and a dispersion of 10.6% (Table 4). Interestingly, the Rh(1)/HAP sample exhibited the highest dispersion (11.6%) with an average size close to 11.6 nm. At high Rh loading the particle sizes presented a marked heterogeneity. Moreover, the addition of 2 wt.% Rh resulted in the deposition of larger particle sizes (16.2 nm) corresponding to a dispersion of 8.3%.

Table 4 also lists the Rh dispersion (D_{chem}), active Rh surface area and average particle size (d_{chem}) for the Rh(x)/HAP catalysts as determined by H_2 chemisorption measurements at 313 K. In this case, the dispersion measured on series of the catalysts seemed to follow this general trend: Rh(0.5)/HAP (17%) > Rh(1)/HAP (9.6%) > Rh(2)/HAP (6.4%). The comparison of these values with those determined by TEM techniques showed slight differences in the case of the Rh(1)/HAP and Rh(2)/HAP catalysts. By contrast, on the Rh(0.5)/HAP catalyst the measured Rh dispersion resulted significantly higher (17%) compared to that determined by TEM techniques (10.6%). This could be explained by a possible presence of a fraction of very small particles accessible to the gas phase; but not detectable by TEM techniques.

On the basis of the Rh surface density, calculated as the number of Rh atoms per support unit surface area, the Rh dispersion values were compared with those corresponding to different supports, reported in the literature [6,7,13,44-46]. According to Fig. S3, the values of the Rh dispersion determined on the Rh(x)/HAP catalysts were in good concordance with the general tendency found for a series of Rh catalysts exhibiting different surface areas.

3.7. Acid-base properties of the Rh(x)/HAP catalysts

The basic properties of the reduced Rh(x)/HAP catalysts were characterised by means of CO_2-TPD techniques. Fig. 7a shows the desorption profiles recorded on the samples after pre-adsorption of CO_2 at 313 K for 1 h and flushed with He at 313 K (2 h). The CO_2-TPD trace for the bare support consisted of three desorption peaks centred at 400, 560 and 850 K, which evidenced the presence of three adsorption sites exhibiting different thermal stability. Rhodium deposition induced significant changes affecting both the amount and the thermal stability of the adsorbed CO_2. At low temperatures, the progressive addition of Rh increased the broadness of the first peak (400 K) and provoked its splitting into two peaks centred at 390 K and 435 K. The latter could be associated with the appearance of new weak adsorption sites. Moreover, the presence of Rh seemed to shift the second desorption peak towards lower temperatures, from 560 K to 520 K, suggesting an apparent weakening of these medium-strength basic sites. At high temperatures, the desorption of CO_2 from the strong basic sites was still peaked at 850 K; however, the corresponding amounts of chemisorbed CO_2 seemed to decrease with the Rh loading.

Table 5 lists quantitative data corresponding to total surface density of the adsorption sites and the distribution of the basic sites classified according to their strength (weak,

medium-strength and strong basic sites). These values were determined by integration of the bands centred at three temperature ranges (390-440 K, 500-600 K and >700 K, respectively). Some relevant conclusions might be drawn from the analysis of these results. Hence, it was found that the deposition of 0.5 wt.% Rh onto the HAP increased the total surface basic sites density from 2.7 to 3.1 μmol_{CO2} m^{-2}. Since the basicity of hydroxyapatite generally increases with an increase in the Ca/P ratio [16], we might reasonably explain the high density of the Rh(0.5)/HAP basic sites by its surface enrichment with the Ca species, as evidenced by XPS. However, at high Rh loadings, 1 wt.% and 2 wt.%, the density substantially decreased since it did not exceed 2.2 and 2 μmol_{CO2} m^{-2}, respectively. It is worth noting that the contribution of the strong basic sites decreased on all Rh samples which represented only 8-9% compared with 19% determined on the HAP bare support. Silvester et al. [33] related the occurrence of strong basic sites to the abundance of OH species on the hydroxyapatite surface. In this sense, we thought that the deposition of Rh induced a dehydroxylation of the support surface which might explain the observed decrease in the amounts of the strong basic sites. Moreover, the effect of increasing the Rh content from 0.5 wt.% to 2 wt.% would mainly be an increase in the weak basic sites fraction at the expense of the medium-strength and strong adsorption sites. Indeed, the weak basic sites represented 26% on the HAP bare support while they accounted for 28% on the Rh/(0.5)/HAP, 44% on the Rh/(1)/HAP and 53% on the Rh/(2)/HAP catalyst.

Finally, the acid properties of the reduced samples were examined by means of NH_3-TPD. Fig. 7b and Table 5 summarise the obtained results. The density of acid sites measured on the bare support (2.3 μmol_{NH3} m^{-2}) was markedly larger than that determined for the rhodium-impregnated samples (1.2-1.5 μmol_{NH3} m^{-2}). The NH_3-TPD

profiles corresponding to all analysed samples consisted of a main desorption peak, assigned to weak acid sites, around 450-470 K.

3.8. Catalytic activity

3.8.1. Partial oxidation of methane (POM)

The POM reaction was carried out over the Rh(x)/HAP catalysts after in-situ reduction at 1000 K. Fig. 8(a-d) shows the corresponding results in terms of CH_4 conversion and H_2, CO and CO_2 yields, respectively, in the temperature range 773-1000 K. It was noticed that, over the whole temperature range, the Rh(1)/HAP sample exhibited the highest catalytic performance. Table 6 compares the catalytic activity of the Rh samples, on the basis of T_{50} values. The reported data pointed out that the activity followed this general trend: Rh(1)/HAP (860 K) > Rh(0.5)/HAP (886 K) > Rh(2)/HAP (910 K).

At 773 K the conversion with the most active catalyst was around 37% and it increased to reach about 52% at 873 K and 72% at 1000 K (Fig. 8a). Likewise, the increase in the reaction temperature promoted the H_2 yield, which attained the highest value (0.62) at 1000 K (Fig. 8b). In parallel, an increase in CO yield could be observed from 0.11 at 773 K to 0.62 at 1000 K (Fig. 8c). By contrast, the values of CO_2 yields decreased with the temperature increase (Fig. 8d). For instance, over the Rh(1)/HAP catalyst the Y_{CO2} decreased from 0.25 at 773 K to 0.1 at 1000 K which suggested a lower contribution of the methane combustion activity. In their study on the activity of Rh/alumina catalysts Wang et al. [47] claimed that CO_2 could be formed from adsorbed CO by fast oxidation with adsorbed oxygen or by the nucleophilic attack of adsorbed hydroxyl. It should be noted that, despite exhibiting the highest metallic surface area (0.55 m^2 g^{-1}), compared with those measured on Rh(0.5)/HAP (0.18 m^2 g^{-1}) and Rh(1)/HAP (0.38 m^2 g^{-1}), the

Rh(2)/HAP showed the poorest performance. Our TEM results revealed that, on the three Rh catalysts, the mean particle sizes followed this trend: Rh(1)/HAP (11.6 nm) < Rh(0.5)/HAP (12.8 nm) < Rh(2)/HAP (16.2 nm). This comparison pointed out the structure sensitivity of the Rh particles spread over the HAP carrier. A comparison of our results with those reported in a previous study [48] showed that lower methane conversion values were obtained over Rh/SiO_2 systems which did not exceed 46% at 873 K (versus 53% over the Rh(1)/HAP catalyst). This comparison proved the potential of HAP support as a good alternative.

Table 6 also lists the obtained H_2/CO and CO/CO_2 ratios calculated at 773 K, 873 K and 973 K over all tested catalysts. The analysis of the H_2/CO values evidenced, irrespective of the used catalyst, an inverse dependence with temperature. Despite this behaviour the H_2/CO values were in all cases higher than 2. This value was sufficiently high to hinder the encapsulation of the metal particles by deposited carbon [1,49]. It is worth noting that the resulted H_2/CO value (2.1) at 973 K is of great importance since it could be suitable for a posterior use. For instance, Fischer-Tropsch synthesis requires an H_2/CO ratio about 2.1 [50]. If not so, the excess hydrogen would have to be separated. On the other hand, according to Table 6, the increase of the CO/CO_2 ratio values with the reaction temperature confirmed, again, the increase in the reforming activity at the expense of the deep oxidation activity.

The catalytic stability of the most active catalysts (Rh(0.5)/HAP and Rh(1)/HAP) was investigated by analysing the evolution of methane conversion and the products yields with time on stream at 973 K for 30 h (Fig. 9). The two catalysts exhibited a very good stability in the studied time on stream. The methane conversion values were around 68% over Rh(0.5)/HAP and 76% over the Rh(1)/HAP catalyst. The latter also kept its superiority in terms of Y_{H2} (0.69 vs. 0.56 over Rh(0.5)/HAP) and Y_{CO} (0.66 vs. 0.53

over Rh(0.5)/HAP). TPO-MS analyses performed in order to determine the amount of carbon accumulated on the used catalysts showed that the deposited carbon masses were lower than 1 wt.%. This was in good agreement with XRD analysis (not shown) of the spent catalysts which confirmed the absence of the signals due to the formation of carbon (graphite). Moreover, the two tested catalysts did not suffer significant changes in their specific surface areas which remained almost constant. From these post-reaction analyses we could explain the stability of the two catalysts by their excellent resistance against coking.

3.8.2. Steam reforming of methane (SRM)

Fig. 10 (a-d) shows the profiles of CH_4 conversion and H_2, CO and CO_2 yields, respectively, as a function of the reaction temperature over the Rh(x)/HAP catalysts. For reference purposes, a commercial Rh/Al_2O_3 catalyst was also tested under similar experimental conditions. Among the three investigated catalysts, supported on HAP, the highest values of methane conversion and the H_2 and CO yields were given over the Rh(1)/HAP. Hence, at 923 K, around 77% CH_4 conversion was achieved. In addition, it also gave the highest values of Y_{H2} (1.37) and Y_{CO} (0.41). These values demonstrated the superiority of the Rh(1)/HAP when compared with those given by a 1%Rh/CeZr catalyst, reported by Rabe et al. [50]. By contrast, the Rh(0.5)/HAP sample showed the poorest performance; even at 973 K, the values corresponding to X_{CH4}, Y_{H2}, Y_{CO} and Y_{CO2} did not exceed 66%, 1.14, 0.33 and 0.33, respectively. It is worth outlining that both conversion and yields achieved with the Rh(1)/HAP catalyst were close to the values obtained over the commercial Rh/Al_2O_3 catalyst. The values of T_{50} were relatively similar on the two tested catalysts (845 K on the former and 830 K on the latter).

A comparison of the performance of the Rh(1)/HAP catalyst in POM and SRM reactions showed that, at low temperatures (< 873 K), replacing oxygen with steam resulted in both lower methane conversion and CO yield while it improved the H_2 production. At high temperatures (≥ 873 K), by contrast, an increase in the overall activity as well as H_2 yield were observed. In parallel, the calculated H_2/CO ratio was, in all investigated temperatures, higher than 5.6 (Table 6). Furthermore, in the presence of steam, the assayed catalysts gave considerable amounts of CO_2 suggesting the main occurrence of water gas shift reaction. For instance, at 973 K, the SRM gas mixture gave Y_{CO2} values ranged between 0.3-0.4 whereas they were lower than 0.15 in the POM process.

In order to investigate the stability of the Rh catalysts in the SRM reaction, additional experiments were carried out, at 973 K, for a considerably more prolonged reaction time interval (30 h) (Fig. 11). As a general behaviour, all samples were markedly stable. The results also evidenced that the Rh(1)/HAP maintained its superiority in terms of catalytic activity and the production of H_2. On the basis of their catalytic activity and H_2 yield the tested catalysts followed this general trend: Rh/Al_2O_3 > Rh(1)/HAP > Rh(2)/HAP > Rh(0.5)/HAP. On the other hand, as checked by XRD and TPO-MS analyses for the post-reaction catalysts, operating with a high H_2O/CH_4 molar ratio (3) did not promote the carbon deposition which might explain their high stability. BET measurements also evidenced that the Rh catalysts did not suffer a significant loss in their surface area. Furthermore, a comparison of the XRD patterns of the freshly reduced and the used catalysts confirmed that there was no alteration of their crystalline structure.

3.9. Discussion

From the analysis of the catalytic data, in both POM and SRM reactions, it is clear that, among all tested Rh/HAP samples, the catalyst with the optimum loading of 1% is the most active one. The better behaviour of this sample might be related to the distribution of the Rh species and the improved textural properties compared to the rest of the catalysts (Rh(0.5)/HAP and Rh(2)/HAP). As shown by the different characterisation techniques, these interesting properties could be provided by an initial distribution of the Rh species, in the freshly calcined sample, characterised by a low contribution of the incorporated Rh species in the HAP structure. This is because the reduction of incorporated Rh provoked a phase transformation from HAP to TCP which significantly lowered the activity of the metallic Rh. In this sense, we thought that the interaction of Rh with TCP phase seemed to have a negative impact on the catalyst activity.

On the other hand, it is worth highlighting the interest of the Rh(1)/HAP sample as an alternative highly active and coke-resistant catalyst to the conventional Rh/Al_2O_3. The former possessed a relatively lower specific surface area (27 $m^2\ g^{-1}$ vs. 125 $m^2\ g^{-1}$ on the Rh/Al_2O_3) and a lower dispersion of Rh (11.6% vs 32% on the Rh/Al_2O_3). Despite this fact the catalytic performance of the Rh(1)/HAP sample in SRM appeared as good as that of the commercial Rh/Al_2O_3. One could attribute this comparable behaviour to suitable properties provided by HAP support such as reducibility, peculiar surface chemistry and some textural properties which might compensate the low dispersion of the Rh active phase induced by its low specific surface area. Indeed, in contrast to alumina, the H_2-TPR results showed that the HAP support exhibited relatively high reducibility with a reversible character. Regarding the acid-base properties, though quantitative information revealed that HAP and alumina supports had comparable basic properties, the difference between them mainly is the number of the acid sites. The alumina (500 $\mu mol_{NH3}\ g^{-1}$) has an overall acidity 8 times larger than the HAP support

(62 μmol_{NH3} g^{-1}). We also thought that, operating at relatively high temperatures, the pore size (42-48 nm) exhibited by the series of the Rh/HAP samples might be beneficial for their catalytic performance. In this sense, these large pore sizes (4 times larger than that of Rh/Al_2O_3, Table 1) could ensure a better diffusion of the reactants and the products during the SRM reaction.

4. Conclusions

Highly active and stable Rh/hydroxyapatite samples prepared by impregnation were investigated for the partial oxidation and steam reforming of methane. The catalysts were analysed by BET, XRD, DRS, XPS, H_2-TPR, TEM, H_2 chemisorption, CO_2-TPD and NH_3-TPD techniques. The characterisation results showed that, after calcination, Rh existed in three different forms in the samples: (i) large crystallites of Rh_2O_3 deposited on the surface of catalysts, (ii) RhO_x in small particles exhibiting strong interaction with the support and (iii) a phase of Rh^{2+} species which incorporated the hydroxyapatite framework. After reduction at 1000 K, the structural and textural properties of the catalysts seemed to depend on the distribution of the Rh among these three different sites. The reduction of the incorporated Rh provoked a phase transformation from HAP to TCP which significantly lowered the specific surface area of the catalysts. However, the catalyst with the lowest contribution of these species (Rh(1)/HAP) showed a good resistance against the loss of its specific surface area due to its higher structural stability.

Operating in the POM and SRM processes the Rh(x)/HAP catalysts resulted highly active and exhibited excellent stability at 973 K in the studied time on stream (30 h). This behaviour was explained by their high coke-resistance. However, the interaction of Rh with TCP phase seemed to have a negative impact on the catalyst activity. The

activity of the catalyst with the optimum loading (1%) was compared with that of a commercial Rh/Al_2O_3 catalyst. The conversion levels and H_2 and CO yields achieved on the former were very close. This comparable behaviour was explained by suitable properties provided by the HAP support such as reducibility, lower surface acidity and larger pore sizes (ensuring a better diffusion of the reactants and the products during the SRM reaction). These properties seemed to compensate the low dispersion of the Rh active phase induced by its low specific surface area.

Acknowledgements

The financial support for this work provided by Ministerio de Economía y Competitividad (CTQ2015-73219-JIN (AEI/FEDER/UE), ENE2013-41187-R and ENE2016-74850-R) and Gobierno Vasco (GIC IT-657-13) is gratefully acknowledged. Likewise, the technical support provided by SGIker (UPV/EHU) is gratefully acknowledged.

References

[1] Z. Boukha, C. Jiménez-González, B. de Rivas, J.R. González-Velasco, J.I. Gutiérrez-Ortiz, R. López-Fonseca, Appl. Catal. B-Environ. 158-159 (2014) 190-201.

[2] Z. Boukha, C. Jiménez-González, M. Gil-Calvo, B. de Rivas, J.R. González-Velasco, J.I. Gutiérrez-Ortiz, R. López-Fonseca, Appl. Catal. B-Environ. 199 (2016) 372-383.

[3] C. Jiménez-González, Z. Boukha, B. de Rivas, J.J. Delgado, M.Á. Cauqui, J.R. González-Velasco, J.I. Gutiérrez-Ortiz, R. López-Fonseca, Appl. Catal. A-Gen. 466 (2013) 9-20.

[4] C. Jiménez-González, Z. Boukha, B. de Rivas, J.R. González-Velasco, J.I. Gutiérrez-Ortiz, R. López-Fonseca, Int. J. Hydrogen Energy 40 (2015) 5281-5288.

[5] B.C. Enger, R. Lødeng, A. Holmen, Appl. Catal. A-Gen. 346 (2008) 1-27.

[6] Z. Hou, P. Chen, H. Fang, X. Zheng, T. Yashima, Int. J. Hydrogen Energy 31 (2006) 555-561.

[7] J. Wei, E. Iglesia, J. Catal. 225 (2004) 116–127.

[8] Y. Liu, W.P. Fang, W.Z. Weng, H..L. Wan, J. Mol. Catal. A. 239 (2005) 193–200.

[9] A. Iulianelli, S. Liguori, J. Wilcox, A. Basile, Catal. Rev. Sci. Eng. 58 (2016) 1-35.

[10] D.A.J.M. Ligthart, R.A. van Santen, E.J.M. Hensen, J. Catal. 280 (2011) 206-220.

[11] O.V. Buyevskaya, D. Wolf, M. Baerns, Catal. Lett. 29 (1994) 249-260.

[12] Z. Tian, O. Dewaele, G.B. Marin, Catal. Lett. 57 (1999) 9-17.

[13] Y. Wang, Y.H. Chin, R.T. Rozmiarek, B.R. Johnson, Y. Gao, J. Watson, A.Y.L. Tonkovich, D.P. Vander Wiel, Catal. Today 98 (2004) 575-581.

[14] Z. Boukha, J.L. Ayastuy, J.R. González-Velasco, M.A. Gutiérrez-Ortiz, Appl. Catal. B-Environ. 201 (2017) 189-201.

[15] Z. Boukha, J. González-Prior, B. de Rivas, J.R. González-Velasco, R. López-Fonseca, J.I. Gutiérrez-Ortiz, J. Ind. Eng. Chem. 57 (2017) 77-88.

[16] Z. Boukha, J. González-Prior, B. Rivas, J.R. González-Velasco, R. López-Fonseca, J.I. Gutiérrez-Ortiz, Appl. Catal. B-Environ. 190 (2016) 125-136.

[17] Z. Boukha, M. Kacimi, M.F.R. Pereira, J.L. Faria, J.L. Figueiredo, M. Ziyad, Appl. Catal. A-Gen. 317 (2007) 299-309.

[18] Z. Boukha, M. Kacimi, M. Ziyad, A. Ensuque, F. Bozon-Verduraz, J. Mol. Catal. A-Chem. 270 (2007) 205-213.

[19] U. Iriarte-Velasco, J.L. Ayastuy, Z. Boukha, R. Bravo, M.Á. Gutierrez-Ortiz, Renew. Energy 115 (2018) 641-648.

[20] A. Borodzinski, M. Bonarowska, Langmuir, 13 (1997) 5613-5620.

[21] H. Kim, L. Li, Y. Koh, J.C. Knowles, H. Kim, J. Am. Ceram. Soc. 87 (2004) 1939-1944.

[22] S.M.M. Zamani, K. Behdinan, Ceram. Int. 43 (2017) 12239-12248.

[23] V.S. Bystrov, C. Piccirillo, D.M. Tobaldi, P.M.L. Castro, J. Coutinho, S. Kopyl, R.C. Pullar, Appl. Catal. B-Environ. 196 (2016) 100-107.

[24] A. Gayen, K.R. Priolkar, P.R. Sarode, V. Jayaram, M. S. Hegde,G. N. Subbanna, S. Emura, Chem. Mater. 16 (2004) 2317-2328.

[25] V. Perrichon, A. Laachir, G. Bergeret, R. Fréty, L. Tournayan, J. Chem. Soc. Faraday Trans. 90 (1994) 773-781.

[26] M.F.L. Johnson, J. Mooi, J. Catal. 103 (1987) 502-505.

[27] H. C. Yao, Y.F.Y. Yao, J. Catal. 86 (1984) 254-265.

[28] E. Ruckenstein, H. Y. Wang, J. Catal. 190 (2000) 32-38.

[29] H. Y. Wang, E. Ruckenstein, J. Catal. 186 (1999) 181-187.

[30] S. Naito, H. Tanaka, S. Kado, T. Miyao, S. Naito, K. Okumura, K. Kunimori, K. Tomishige, J. Catal. 259 (2008) 138-146.

[31] M.J. Rice, A.K. Chakraborty, A.T. Bell, J. Phys. Chem. B. 104 (2000) 9987-9992.

[32] Z. Weng-Sieh, R. Gronsky, A.T. Bellz, J. Catal. 170 (1997) 62-74.

[33]L. Silvester, J. Lamonier, R. Vannier, C. Lamonier, M.Capron, A. Mamede, F. Pour point, A. Gervasini, F.Dumeignil, J. Mater. Chem. A. 2 (2014) 11073-11090.

[34] Yoshio Abe, Kiyohiko Kato, Midori Kawamura, and Katsutaka Sasaki, Surf. Sci. Spectra 8 (2001) 117-125.

[35] R. Konta, T. Ishii, H. Kato, A. Kudo, J. Phys. Chem. B. 108 (2004) 8992-8995

[36] R.L. Oliveira, I.G. Bitencourt, F.B. Passos, J. Braz. Chem. Soc. 24 (2013) 68-75.

[37] M. Kaczmarek, R.W. Eason, I. Mnushkina, Appl. Phys. B. 68 (1999) 813-817.

[38] K. Iwashina, A. Kudo, J. Am. Chem. Soc. 133 (2011) 13272-13275.

[39] S. Okunaka, H. Tokudome, R. Abe, J. Mater. Chem. A. 3 (2015) 14794-14800.

[40] V.O. Stoyanovskii, A.A. Vedyagin, G.I. Aleshina, A.M. Volodin, A.S. Noskov, Appl. Catal. B-Environ. 90 (2009) 141-146.

[41] E.N.K. Glover, S.G. Ellington, G. Sankar and R.G. Palgrave, J. Mater. Chem. A. 4 (2016) 6946-6954.

[42] S. Kawasaki, K. Akagi, K. Nakatsuji, S. Yamamoto et al. J. Phys. Chem. C 116 (2012) 24445-24448.

[43] C. Görller-Walrand, B. Gilliams, J. D'Olieslager, Chem. Phys. Lett. 246 (1995) 163-166.

[44] S. Eriksson, A. Schneider, J. Mantzaras, M. Wolf, S. Järåsa, Chem. Eng. Sci. 62 (2007) 3991-4011.

[45] L. Qian, B. Yue, S. Pei, L. Zhang, L. Ye, J. Cheng, S.C. Tsang, H. He, Chin. J. Chem. 28 (2010) 1864-1870.

[46] D. Laprune, C. Theodoridi, A. Tuel, D. Farrusseng, F.C. Meunier, Appl. Catal. B-Environ. 204 (2017) 515-524

[47] D. Wang, O. Dewaele, A.M. De Groote, G.F. Froment, J. Catal. 159 (1996) 418-426.

[48] C. Mateos-Pedrero, C. Cellier, P. Ruiz, Catal. Today 117 (2006) 362-368.

[49] C.H. Bartholomew, Appl. Catal. A-Gen. 212 (2001) 17-60.

[50] S. Rabe, T. Truong, F. Vogel, Appl. Catal. A-Gen. 292 (2005) 177-188.

CAPTIONS FOR TABLES AND FIGURES

Table 1 N_2 physisorption and XRD data corresponding to Rh(x)/HAP catalysts.

Table 2 H_2-TPR data for the Rh(x)/HAP catalysts.

Table 3 XPS data for Rh(x)/HAP catalysts.

Table 4 TEM and H_2 chemisorption data of the Rh(x)/HAP catalysts.

Table 5 Data of NH_3-TPD and CO_2-TPD studies over the Rh(x)/HAP samples.

Table 6 T_{50}, H_2/CO and CO/CO_2 ratios in POM and SRM reactions over the Rh(x)/HAP catalysts. Data corresponding to the commercial Rh/Al_2O_3 catalyst and thermodynamic equilibrium were also included.

Figure 1 Pore size distribution for the (-c) calcined and (-r) reduced catalysts

Figure 2 XRD patterns for the (-c) calcined and (-r) reduced Rh(x)/HAP catalysts

Figure 3 H_2-TPR profiles of the Rh(x)/HAP catalysts.

Figure 4 XPS spectra corresponding to $3d_{3/2}$-$3d_{5/2}$ region for the Rh(x)/HAP catalysts.

Figure 5 DRS spectra for the Rh(x)/HAP catalysts.

Figure 6 TEM micrographs and Rh particle size distribution for the reduced (a) Rh(0.5)/HAP, (b) Rh(1)/HAP and (c) Rh(2)/HAP catalysts.

Figure 7 (a) CO_2-TPD and (b) NH_3-TPD profiles of the Rh(x)/HAP catalysts.

Figure 8 Methane conversion (a) and H_2 (b), CO (c) and CO_2 (d) yields over reduced Rh(x)/HAP catalysts versus reaction temperature in the POM reaction. Reaction conditions: 19,200 cm^3 CH_4 g^{-1} h^{-1}; W = 0.250 g. Gas mixture: 10%CH_4/5%O_2/N_2.

Figure 9 Activity and products distribution over reduced Rh(0.5)/HAP and Rh(1)/HAP catalysts versus time on stream in the POM reaction. Reaction conditions: 19,200 cm^3 CH_4 g^{-1} h^{-1}; W = 0.250 g, T = 973 K. Gas mixture: 10%CH_4/5%O_2/N_2.

Figure 10 Methane conversion (a) and H_2 (b), CO (c) and CO_2 (d) yields over reduced Rh(x)/HAP catalysts versus reaction temperature in the SRM reaction. Reaction conditions: 19,200 cm^3 CH_4 g^{-1} h^{-1}; W = 0.250 g. Gas mixture: 10%CH_4/30%H_2O/N_2. Data corresponding to the commercial Rh/Al_2O_3 catalyst were also included.

Figure 11 Methane conversion (a) and H_2 (b), CO (c) and CO_2 (d) yields over reduced Rh(x)/HAP catalysts versus time on stream in the SRM reaction. Reaction conditions: 19,200 cm^3 CH_4 g^{-1} h^{-1}; W = 0.250 g; T = 973 K. Gas mixture:

10%CH_4/30%H_2O/N_2. Data corresponding to the commercial Rh/Al_2O_3 catalyst and thermodynamic equilibrium were also included.

Catalysts	S_{BET}, $m^2 g^{-1}$	Vp, $cm^3 g^{-1}$	dp, nm	(a ± 0.02), Å	(c ± 0.002), Å	V, $Å^3$	d_{HAP}, nm[c]
HAP	30[a] 33[b]	0.29 0.30	38 33	9.3701 9.3692	6.8188 6.8144	518.5 518.0	49 32
Rh(0.5)/HAP	31[a] 26[b]	0.29 0.27	36 40	9.3845 9.3810	6.8216 6.8181	520.3 519.6	44 47
Rh(1)/HAP	31[a] 30[b]	0.26 0.30	32 37	9.3965 9.3974	6.8168 6.8073	521.2 520.6	39 43
Rh(2)/HAP	30[a] 25[b]	0.27 0.24	35 37	9.4314 9.4328	6.7945 6.7948	523.4 523.6	37 39
Rh/Al_2O_3	132[a] 125[b]	0.42 0.35	10 9				

(a) Samples calcined at 1000 K.
(b) Samples reduced at 1000 K.
(c) HAP crystallite size calculated according to Scherrer equation.

Table 1

Catalysts	Total reducibility, $\mu mol_{H2}\ g^{-1}$	Rh reducibility, $\mu mol_{H2}\ g^{-1(a)}$	H_2/Rh	Reducibility of the Rh species		
				α, $\mu mol_{H2}\ g^{-1(b)}$	β, $\mu mol_{H2}\ g^{-1(b)}$	γ, $\mu mol_{H2}\ g^{-1(b)}$
HAP	209	0	-	0	0	0
Rh(0.5)/HAP	289	62	1.2	31 (50%)[c]	15 (24%)	16 (26%)
Rh(1)/HAP	360	115	1.2	60 (52%)	35 (31%)	20 (17%)
Rh(2)/HAP	507	256	1.3	141 (55%)	59 (23%)	56 (22%)

(a) As determined by integration of the peaks assigned to Rh species (Fig. 3).
(b) As determined by integration of the peak assigned to each Rh species (Fig. 3).
(c) Values in brackets correspond to the contribution of this phase to the total amounts of consumed H_2.

Table 2

Catalysts	XPS							
	Rh,% (ICP)	Rh, % (XPS)	Ca/P	Rh ($3d_{5/2}$), eV	Rh ($3d_{3/2}$), eV	Ca 2p, eV	P 2p, eV	O 1s, eV
HAP	0	0	1.5	-	-	346.8	133.4	530.8
Rh(0.5)/HAP	0.5	0.5	1.6	307.9	312.6	346.2	133.9	530.0
Rh(1)/HAP	1.0	0.9	1.5	307.8	312.4	346.2	134.6	530.1
Rh(2)/HAP	2.0	1.4	1.5	307.7	312.2	346.0	134.3	530.2

Table 3

Catalysts	TEM			H_2 chemisorption		
	d_{TEM}, nm[(a)]	D_{TEM}, %[(a)]	S_{Rh}, $m^2 g^{-1}$[(a)]	d_{chem}, nm[(b)(c)]	D_{chem}, %[(b)]	S_{Rh}, $m^2 g^{-1}$[(b)]
Rh(0.5)/HAP	12.8	10.6	0.18	7.9	17	0.28
Rh(1)/HAP	11.6	11.6	0.38	14	9.6	0.32
Rh(2)/HAP	16.2	8.3	0.55	21.1	6.4	0.42
Rh/Al_2O_3	-	-	-	3.6	32	1.06

(a) As determined by TEM techniques.
(b) As determined by H_2 chemisorption experiments at 313 K.
(c) Calculated according to Eq. (3) and Eq. (4).

Table 4

Catalysts	Surface acidity, $\mu mol_{NH3}\ m^{-2}$	Surface basicity, $\mu mol_{CO2}\ m^{-2}$	Weak basic sites, % (390-440 K)	Medium basic sites, % (500-600 K)	Strong basic sites, % (> 700 K)
HAP	2.3	2.7	26	55	19
Rh(0.5)/HAP	1.2	3.1	28	63	9
Rh(1)/HAP	1.2	2.2	44	47	9
Rh(2)/HAP	1.5	2.0	53	39	8

Table 5

Reaction	Catalyst	T_{50}, K	H_2/CO			CO/CO_2		
			773 K	873 K	973 K	773 K	873 K	973 K
POM	Rh(0.5)/HAP	886	3.4	2.6	2.1	0.2	1.1	3.8
	Rh(1)/HAP	860	3.4	2.5	2.1	0.5	1.5	4.6
	Rh(2)/HAP	910	2.6	3.1	2.1	0.4	0.4	4.2
	Equilibrium	850	10.8	3.7	2.3	0.5	2.4	14.7
SRM	Rh(0.5)/HAP	910	19.4	10.8	6.9	0.2	0.5	1.0
	Rh(1)/HAP	845	19.9	8.9	5.8	0.2	0.7	1.5
	Rh(2)/HAP	860	19.9	9.9	6.4	0.2	0.5	1.1
	Rh/Al_2O_3	830	21.6	9.4	5.6	0.2	0.6	1.2
	Equilibrium	750	21.1	8.2	5.9	0.2	0.8	1.4

Table 6

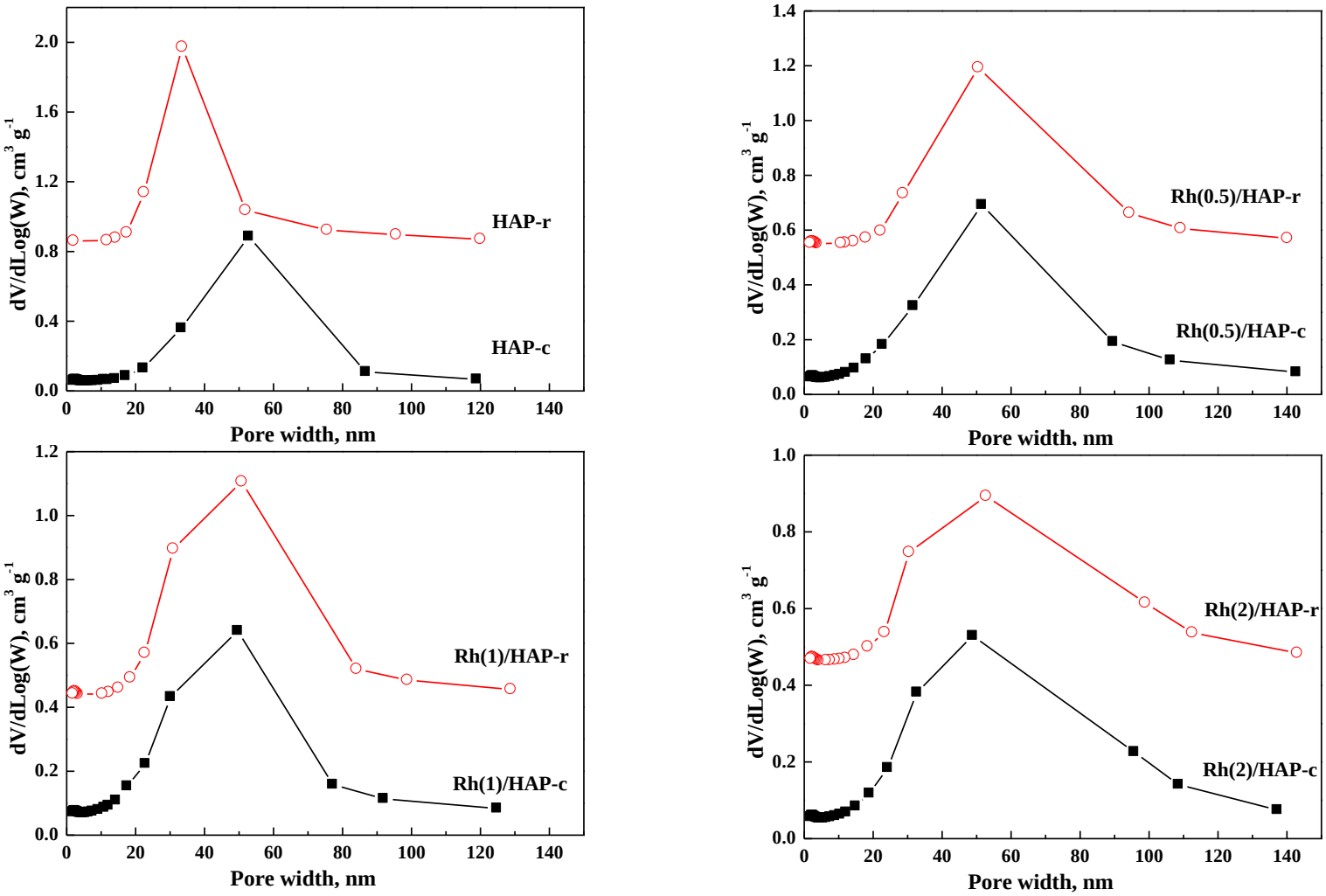
dV/dLog(W), cm3 g-1
Pore width, nm
HAP-r
HAP-c
Rh(0.5)/HAP-r
Rh(0.5)/HAP-c
Rh(1)/HAP-r
Rh(1)/HAP-c
Rh(2)/HAP-r
Rh(2)/HAP-c

Figure 1

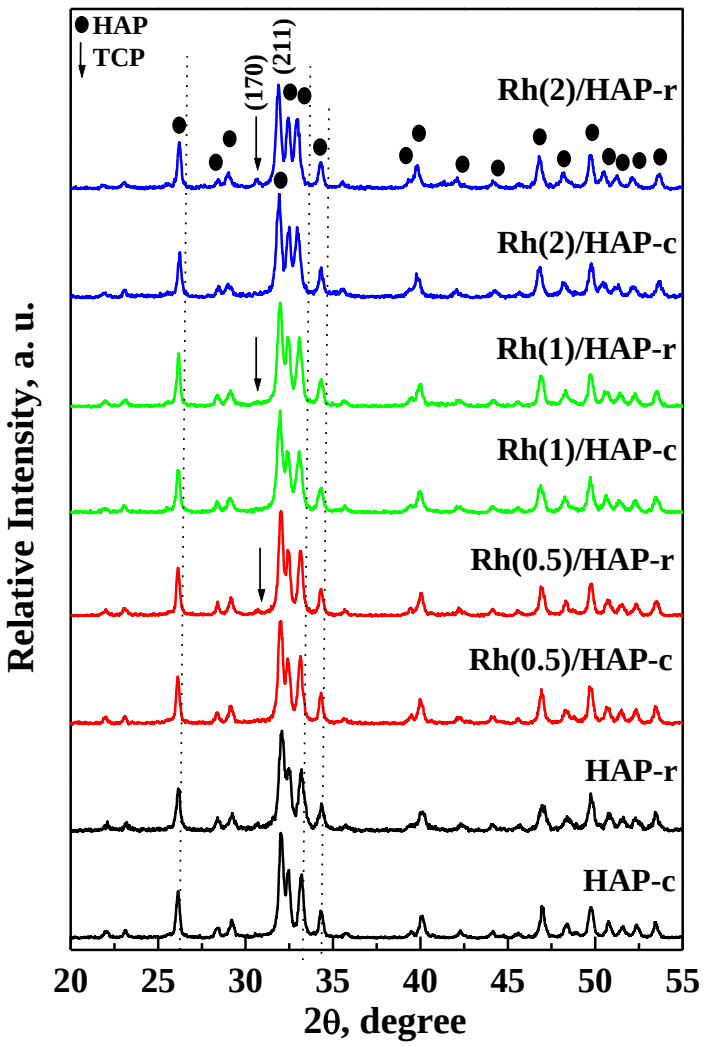
HAP
TCP
(170)
(211)
Rh(2)/HAP-r
Rh(2)/HAP-c
Rh(1)/HAP-r
Rh(1)/HAP-c
Rh(0.5)/HAP-r
Rh(0.5)/HAP-c
HAP-r
HAP-c
Relative Intensity, a. u.
20
25
30
35
40
45
50
55
2θ, degree

Figure 2

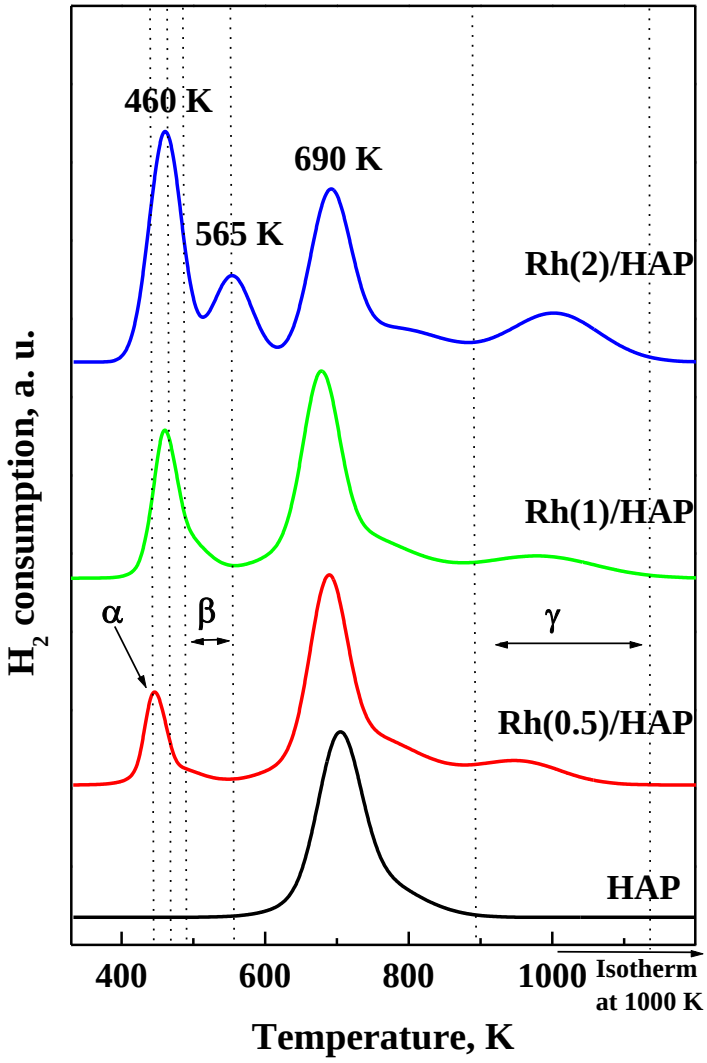
460 K
690 K
565 K
Rh(2)/HAP
Rh(1)/HAP
α
β
γ
Rh(0.5)/HAP
HAP
400
600
800
1000
Isotherm
at 1000 K
Temperature, K
H2 consumption, a. u.

Figure 3

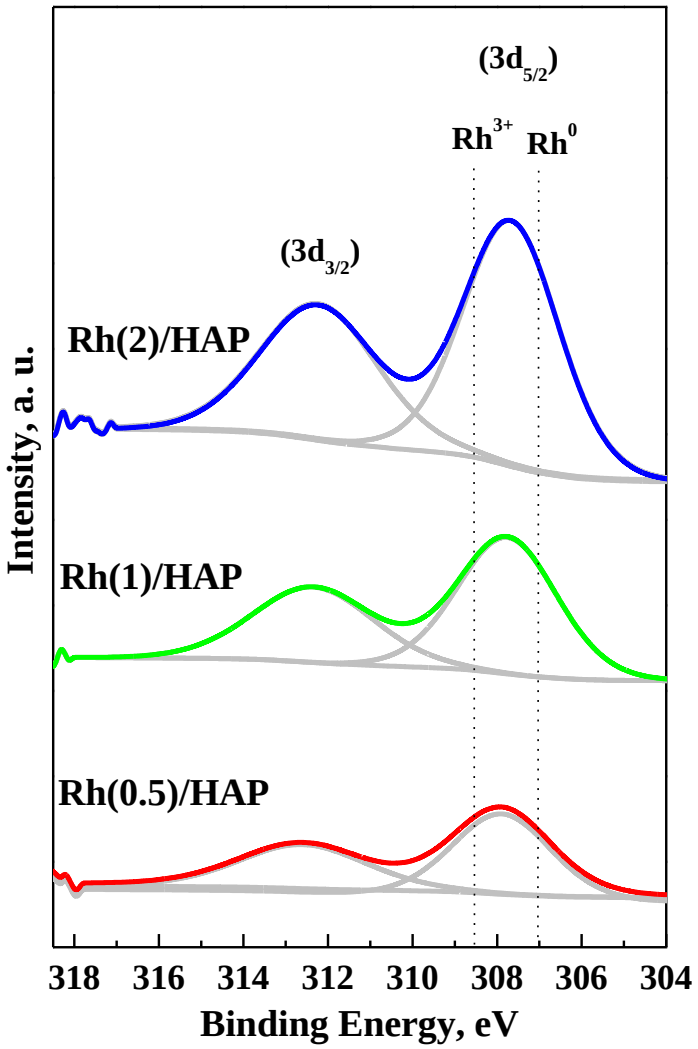
(3d5/2)
Rh3+
Rh0
(3d3/2)
Rh(2)/HAP
Rh(1)/HAP
Rh(0.5)/HAP
Intensity, a. u.
318
316
314
312
310
308
306
304
Binding Energy, eV

Figure 4

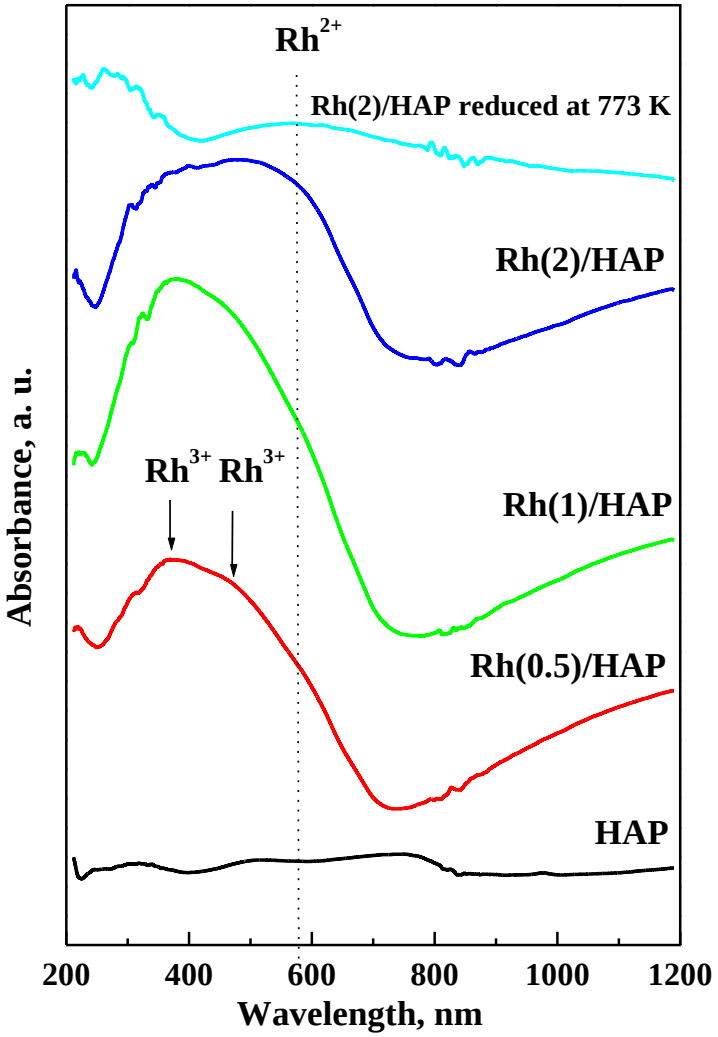
Rh2+
Rh(2)/HAP reduced at 773 K
Rh(2)/HAP
Rh3+ Rh3+
Rh(1)/HAP
Rh(0.5)/HAP
HAP
Absorbance, a. u.
200
400
600
800
1000
1200
Wavelength, nm

Figure 5

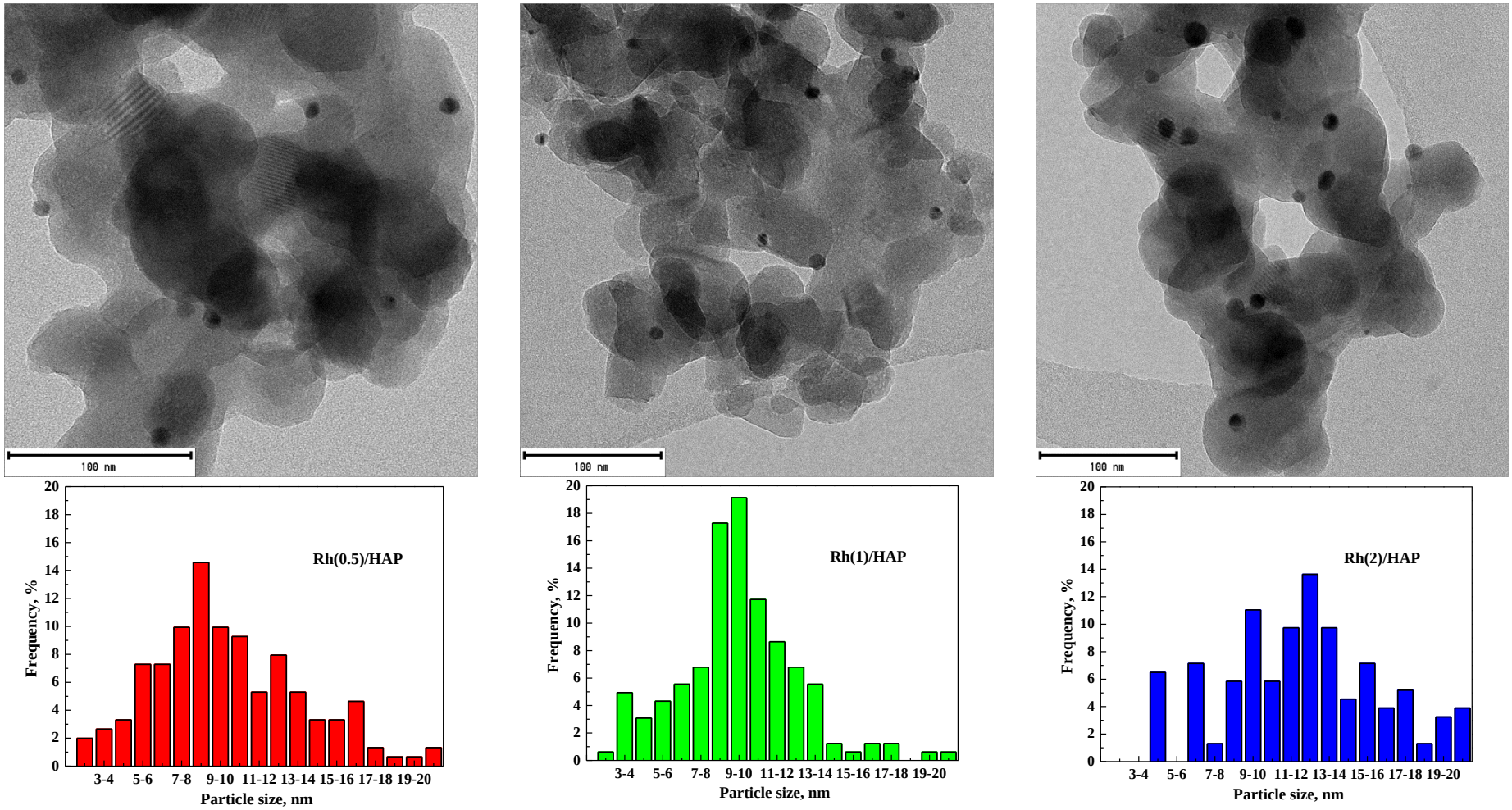
100 nm
100 nm
100 nm
Rh(0.5)/HAP
Rh(1)/HAP
Rh(2)/HAP
Frequency, %
Particle size, nm
0
2
4
6
8
10
12
14
16
18
20
3-4
5-6
7-8
9-10
11-12
13-14
15-16
17-18
19-20

(a) **(b)** **(c)**

Figure 6

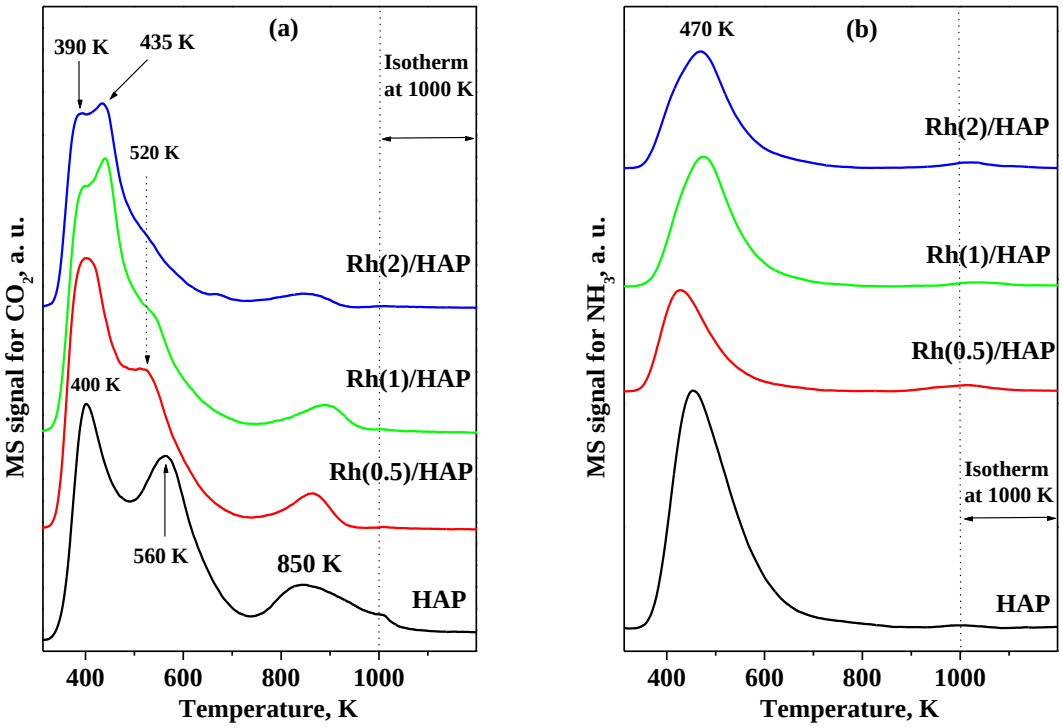
(a)
390 K
435 K
520 K
400 K
560 K
850 K
Isotherm
at 1000 K
Rh(2)/HAP
Rh(1)/HAP
Rh(0.5)/HAP
HAP
MS signal for CO2, a. u.
400
600
800
1000
Temperature, K
(b)
470 K
Rh(2)/HAP
Rh(1)/HAP
Rh(0.5)/HAP
Isotherm
at 1000 K
HAP
MS signal for NH3, a. u.
400
600
800
1000
Temperature, K

Figure 7

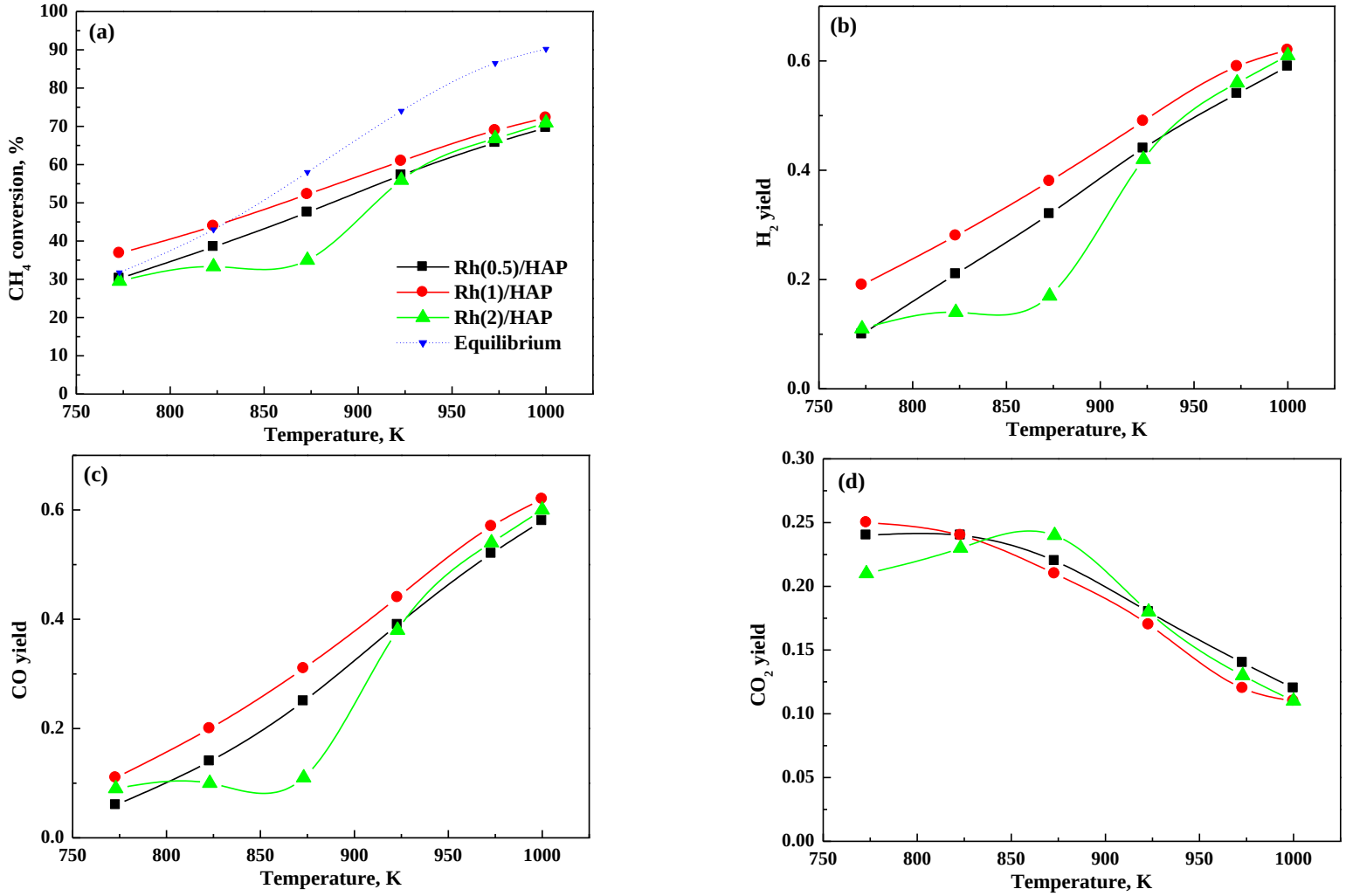
(a)
CH4 conversion, %
Temperature, K
Rh(0.5)/HAP
Rh(1)/HAP
Rh(2)/HAP
Equilibrium
(b)
H2 yield
Temperature, K
(c)
CO yield
Temperature, K
(d)
CO2 yield
Temperature, K

Figure 8

1

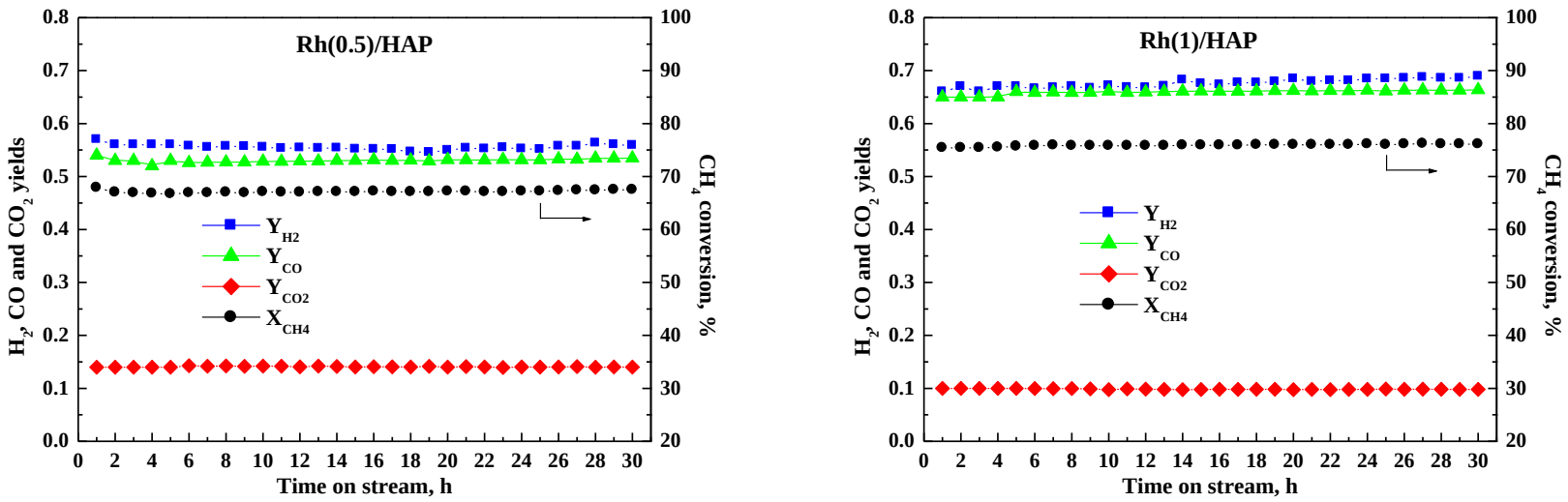
Rh(0.5)/HAP
Rh(1)/HAP
H2, CO and CO2 yields
CH4 conversion, %
Time on stream, h
YH2
YCO
YCO2
XCH4

Figure 9

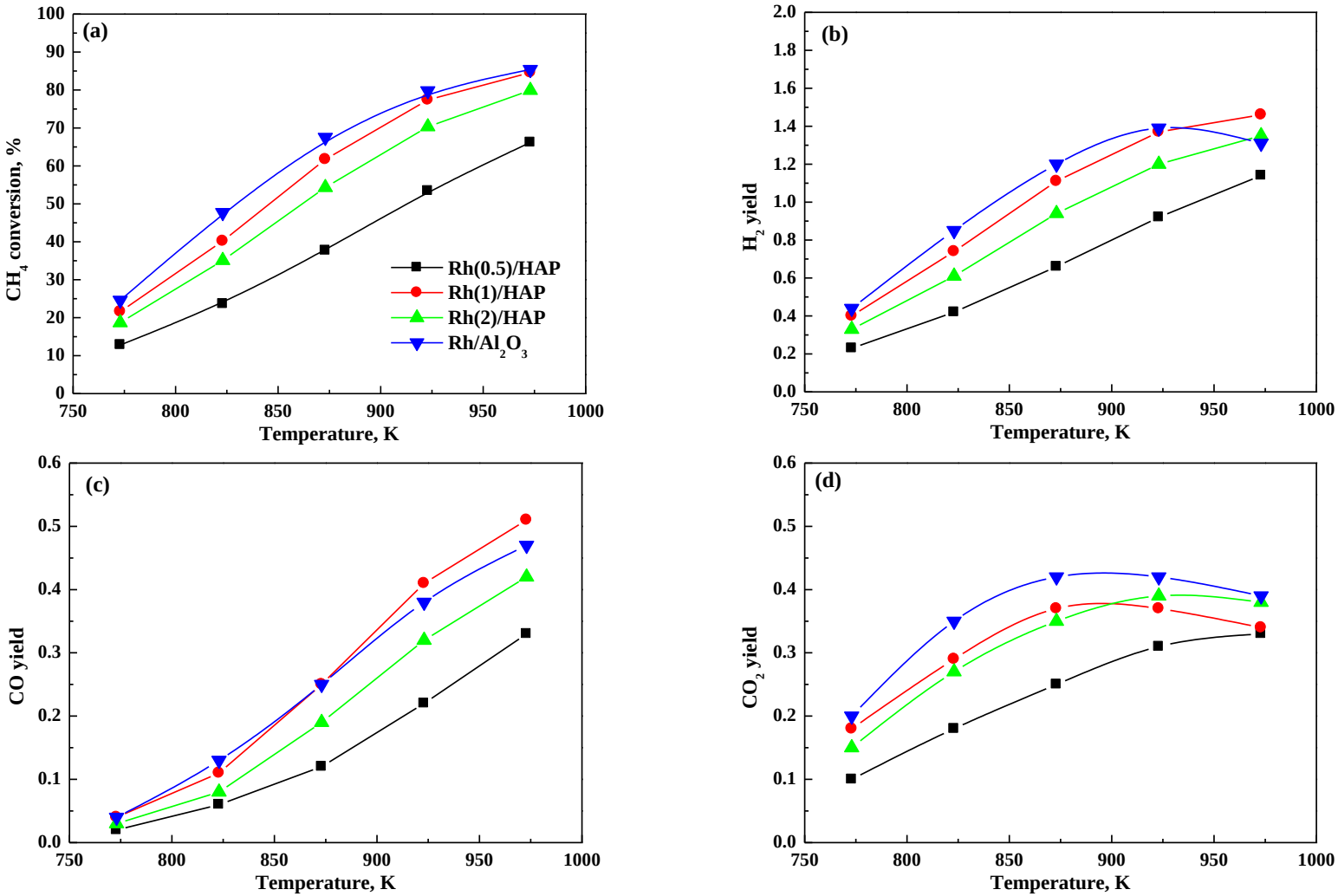
(a)
CH4 conversion, %
Temperature, K
Rh(0.5)/HAP
Rh(1)/HAP
Rh(2)/HAP
Rh/Al2O3
(b)
H2 yield
Temperature, K
(c)
CO yield
Temperature, K
(d)
CO2 yield
Temperature, K

Figure 10

1

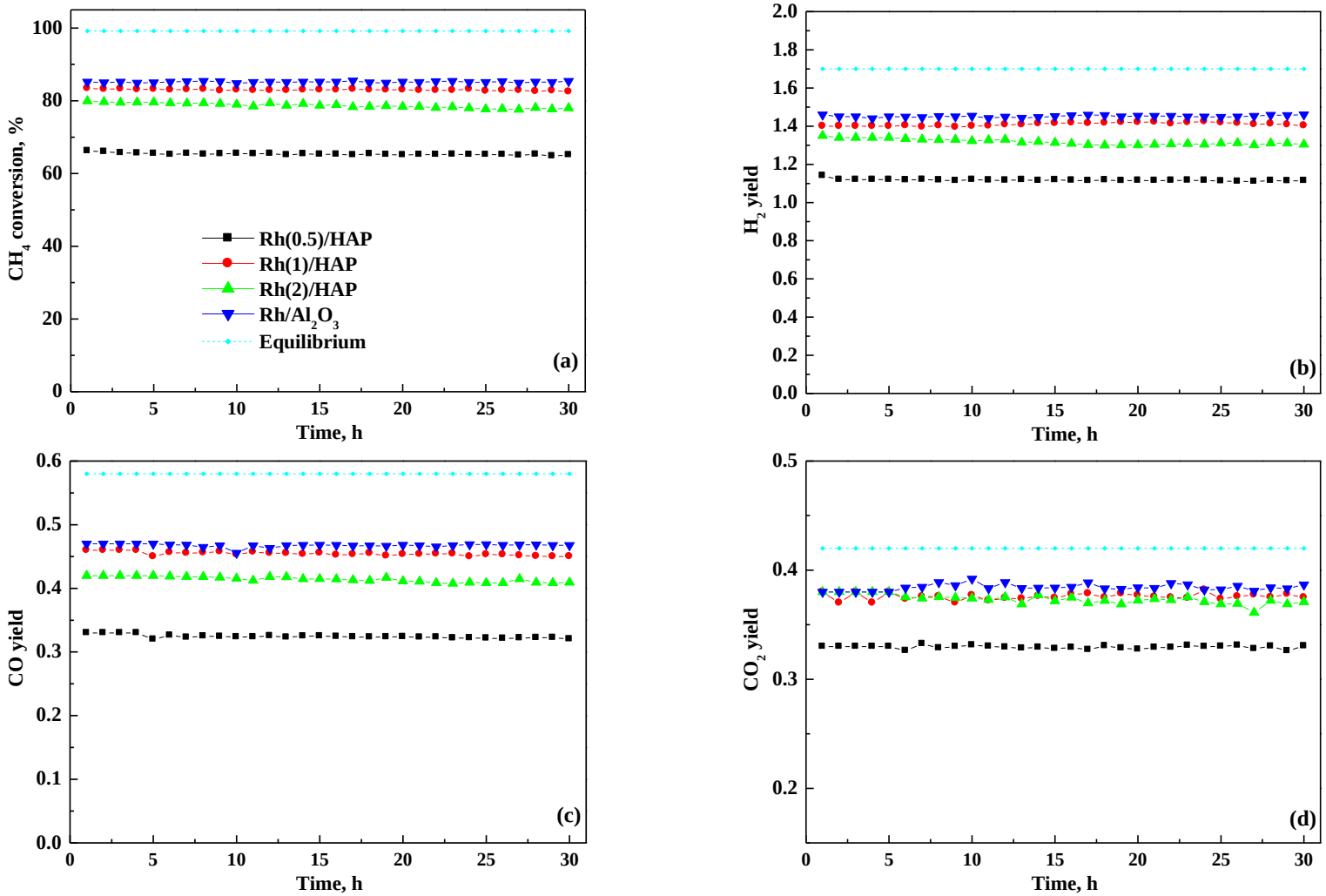
CH4 conversion, %
Time, h
Rh(0.5)/HAP
Rh(1)/HAP
Rh(2)/HAP
Rh/Al2O3
Equilibrium
(a)
H2 yield
(b)
CO yield
(c)
CO2 yield
(d)

Figure 11

1

Supplementary Material

Click here to download Supplementary Material: Supporting information 01-02-2018.pdf